

Article

## Dislocations in SrTiO<sub>3</sub>: easy to reduce but not so fast for oxygen transport

Dario Marocchelli, Lixin Sun, and Bilge Yildiz

*J. Am. Chem. Soc.*, Just Accepted Manuscript • DOI: 10.1021/ja513176u • Publication Date (Web): 09 Mar 2015

Downloaded from <http://pubs.acs.org> on March 14, 2015

### Just Accepted

"Just Accepted" manuscripts have been peer-reviewed and accepted for publication. They are posted online prior to technical editing, formatting for publication and author proofing. The American Chemical Society provides "Just Accepted" as a free service to the research community to expedite the dissemination of scientific material as soon as possible after acceptance. "Just Accepted" manuscripts appear in full in PDF format accompanied by an HTML abstract. "Just Accepted" manuscripts have been fully peer reviewed, but should not be considered the official version of record. They are accessible to all readers and citable by the Digital Object Identifier (DOI®). "Just Accepted" is an optional service offered to authors. Therefore, the "Just Accepted" Web site may not include all articles that will be published in the journal. After a manuscript is technically edited and formatted, it will be removed from the "Just Accepted" Web site and published as an ASAP article. Note that technical editing may introduce minor changes to the manuscript text and/or graphics which could affect content, and all legal disclaimers and ethical guidelines that apply to the journal pertain. ACS cannot be held responsible for errors or consequences arising from the use of information contained in these "Just Accepted" manuscripts.



**ACS Publications**

High quality. High impact.

Journal of the American Chemical Society is published by the American Chemical Society. 1155 Sixteenth Street N.W., Washington, DC 20036  
Published by American Chemical Society. Copyright © American Chemical Society.  
However, no copyright claim is made to original U.S. Government works, or works  
produced by employees of any Commonwealth realm Crown government in the course  
of their duties.

# Dislocations in SrTiO<sub>3</sub>: easy to reduce but not so fast for oxygen transport

Dario Marrocchelli<sup>1</sup>, Lixin Sun<sup>1</sup> and Bilge Yildiz<sup>1,2\*</sup>

<sup>1</sup>Laboratory for Electrochemical Interfaces, Department of Nuclear Science and Engineering, Massachusetts Institute of Technology, 77 Massachusetts Ave., Cambridge, MA 02139, USA

<sup>2</sup>Department of Materials Science and Engineering, Massachusetts Institute of Technology, 77 Massachusetts Avenue, Cambridge, MA 02139, USA

\*byildiz@mit.edu

## Abstract

The effect of dislocations on the chemical, electrical and transport properties in oxide materials is important for electrochemical devices, such as fuel cells and resistive switches, but these effects have remained largely unexplored at the atomic level. In this work, by using large-scale atomistic simulations, we uncover how a <100>{011} edge dislocation in SrTiO<sub>3</sub>, a prototypical perovskite oxide, impacts the local defect chemistry and oxide ion transport. We find that, in the dilute limit, oxygen vacancy formation energy in SrTiO<sub>3</sub> is lower at sites close to the dislocation core, by as much as 2 eV compared to that in the bulk. We show that the formation of a space-charge zone based on the redistribution of charged oxygen vacancies can be captured quantitatively at atomistic level by mapping their formation energies around the dislocation. Oxide-ion diffusion was studied for a low vacancy concentration regime (ppm level) and a high vacancy concentration regime (up to 2.5%). In both cases, no evidence of pipe-diffusion, i.e. significantly enhanced mobility of oxide ions, was found as determined from the calculated migration barriers, contrary to the case in metals. However, in the low vacancy concentration regime, the vacancy accumulation at the dislocation core gives rise to a higher diffusion coefficient, even though the oxide-ion mobility itself is lower than that in the bulk. Our findings have important implications for applications of perovskite oxides for information and energy technologies. The observed lower oxygen vacancy formation energy at the dislocation core provides a quantitative and direct explanation for the electronic conductivity of dislocations in SrTiO<sub>3</sub> and related oxides studied for red-ox based resistive switching. Reducibility and electronic transport at dislocations can also be quantitatively engineered into active materials for fuel cells, catalysis and electronics.

## 1. Introduction

Dislocations are ubiquitous one-dimensional defects found in crystalline materials, including bulk,<sup>1,2</sup> thin film,<sup>3–6</sup> 2-D<sup>7</sup> and nanoscale structures.<sup>7–9</sup> As such, they can affect the properties of materials used in every

technological application, including solid oxide fuel cells (SOFCs),<sup>10</sup> catalysis,<sup>11</sup> resistive switching memories,<sup>12</sup> sensors,<sup>13</sup> Li-ion batteries,<sup>14</sup> photovoltaics,<sup>15</sup> thermoelectrics<sup>16</sup> and multiferroics.<sup>17</sup> Metal oxides in the form of thin films – often used in strain engineering of relevant properties<sup>5</sup> – show especially high concentrations of dislocations.<sup>3,6,18,19</sup> However, despite their ample presence, the effect of dislocations on the electrical,<sup>20,21</sup> chemical<sup>21–23</sup> and transport<sup>20,22,24</sup> properties in oxides is only scarcely explored at a local level. This is contrary to the maturity of knowledge on the compositional and diffusional properties of dislocations in metals.<sup>25–28</sup> In this paper, by using atomistic simulations, we uncover how an edge dislocation in SrTiO<sub>3</sub> (a model and technologically relevant perovskite oxide) impacts the chemical and electrical properties of this material. We provide this work also as an illustrative example to coupled electro-chemo-mechanical behavior in oxides,<sup>5,29</sup> of interest to energy<sup>30,31</sup> and information technologies.<sup>2,12,32,33</sup>

The most prominent phenomenon tied explicitly to dislocations in SrTiO<sub>3</sub> is red-ox based Resistive Switching. Resistive switching is the ability of certain materials, such as SrTiO<sub>3</sub>, to change their resistance state upon the application of an electric bias - a property that can enable high performance memories.<sup>12</sup> To date, several mechanisms have been suggested to explain the origins of this phenomenon.<sup>2,12,20,34–37</sup> Perhaps the most convincing explanation comes from Szot and co-authors, who recently reviewed an impressive amount of literature and suggested that the electrical conductivity of this material under electrical bias is determined by the electrical properties of dislocations.<sup>2</sup> The hypothesis of the work in ref. 2 is that “*the extended dislocation acts as (pipe) diffusion path allowing preferential exchange of oxygen with the surroundings*” under electric field, and thus the dislocations are preferentially reduced. Reduction of the SrTiO<sub>3</sub> along the dislocation, in turn, increases the electronic conductivity of this material<sup>20,38–40</sup> because of the lowering of the oxidation state of Ti ions, from 4+ to 3+, as also supported by theoretical studies.<sup>41–43</sup> The higher conductivity of dislocations upon switching in SrTiO<sub>3</sub> has been demonstrated with Locally-Conducting Atomic Force Microscopy (LC-AFM) experiments,<sup>2,12,44</sup> that show the formation of conducting filaments attributed to dislocations embedded in an insulating matrix. However, the key question is: *what is really the mechanism for the preferential exchange of oxygen at dislocations: is it a thermodynamic factor (i.e. a lower oxygen vacancy formation energy) or is it a kinetic factor (i.e. preferential migration and exchange of oxygen along dislocations)?* Knowing the answers to this question quantitatively would help develop more accurate models for resistive switching kinetics.

A related question is the role of dislocations on the oxide ion conductivity of oxides. This is relevant because previous work have speculated that the RS behavior of SrTiO<sub>3</sub> can be explained in terms of fast oxygen diffusion along a dislocation.<sup>12,34,44,45</sup> Furthermore, other applications of oxides which rely on

oxygen exchange and oxygen transport, such as solid oxide fuel cells, separation membranes and sensors, can benefit from structures that allow for fast oxide ion diffusion.<sup>46</sup> While dislocations are known to facilitate diffusion in metals by enhancing mobility, a phenomenon called *pipe-diffusion*,<sup>25–28</sup> conduction of ions along dislocations in oxides is neither widely quantified nor agreed upon. Some researchers provide evidence that dislocations enhance<sup>19,47</sup> and some suggest that they impede<sup>3,20,22</sup> the mobility of oxide ions in SrTiO<sub>3</sub> and in other oxide materials. *So, do dislocations contribute to the resistive switching process through faster ionic conduction, or is only electronic conduction that plays a role?* Recently, Metlenko et al. performed tracer diffusion and electrical conductivity measurements on SrTiO<sub>3</sub>.<sup>20</sup> They found no evidence of fast diffusion along a dislocation array in a tilt grain boundary, though they could not exclude this possibility because of the limited sensitivity of the experimental approach. Their results were supplemented by a few static calculations of select migration paths and energy barriers, which showed no evidence of increased *mobility* of oxide ions along the dislocation. However, we note here that the diffusion coefficient depends both on the *mobility* and the *concentration* of oxygen defects, as shown by the following formula:<sup>48</sup>

$$D(T) = [V_O^{\bullet}] \gamma a_0^2 \theta e^{-\frac{E_m}{k_B T}} = D_0(T) e^{-\frac{E_m}{k_B T}} \quad \text{with} \quad [V_O^{\bullet}] \propto e^{-\frac{E_f^V}{k_B T}} \quad (1)$$

where  $D$  is the diffusion coefficient,  $[V_O^{\bullet}]$  is the concentration of oxygen vacancies,  $\gamma$  is a constant,  $a_0$  and  $\theta$  are the jump distance and frequency,  $E_m$  is the oxide ion migration energy barrier,  $k_B$  is the Boltzmann constant and  $T$  is the temperature.  $D_0(T)$  contains  $\gamma$ ,  $a_0$  and  $\theta$ , and the vacancy concentration  $[V_O^{\bullet}]$ . We note that the vacancy concentration is itself a function of temperature as it is proportional to  $\exp(-E_f^V/k_B T)$ , where  $E_f^V$  is the oxygen vacancy formation energy. Equation (1) therefore sets the stage for this paper, by showing that the oxide ion diffusion coefficient,  $D$ , depends both on mobility, via  $\exp(-E_m/k_B T)$ , and on the concentration of oxygen defects,  $[V_O^{\bullet}]$ , via  $\exp(-E_f^V/k_B T)$ . We recall here that pipe-diffusion implies a higher mobility, i.e. a lower migration energy barrier,  $E_m$ .<sup>28</sup> However, even if  $E_m$  is higher along the dislocation compared to that in bulk SrTiO<sub>3</sub>, one could still obtain a higher diffusion coefficient,  $D$ , along a dislocation by increasing  $[V_O^{\bullet}]$  due to a reduction in the formation energy of oxygen vacancies. To deduce whether the diffusion coefficient of oxygen can be larger along dislocations in SrTiO<sub>3</sub>, *both* the concentration and mobility terms will be explicitly assessed in the vicinity of the dislocation for the first time in this paper.

Driven by the above motivations, in this paper we use atomistic simulations to address two key questions:

1) *is it easier to create oxygen vacancies (i.e. is it easier to reduce SrTiO<sub>3</sub>) near a dislocation, and by how*

much compared to the bulk  $\text{SrTiO}_3$ ? , and 2) do dislocations enhance the oxide ion conductivity, or diffusion coefficient, in  $\text{SrTiO}_3$ ? As a result, we find that  $\text{SrTiO}_3$  can be easily reduced at the dislocation core due to the under-coordination of oxide ions, with the oxygen vacancy formation energy being up to 2.0 eV lower than the bulk. No evidence of pipe-diffusion, i.e. enhanced oxide ion mobility, was found neither in a low vacancy concentration regime (ppm level) nor in a high vacancy concentration regime (up to 2.5%). However, for the case of low vacancy concentration, we found vacancy accumulation at the dislocation core, which in turn gives rise to a higher diffusion coefficient even though the oxide ion mobility is lower than that in the bulk. The extent of this vacancy accumulation can be impacted kinetically by temperature and dislocation density.

## 2. Methodology

In this section, we briefly present the methodology employed in this work. For the sake of brevity, we report some technical details in the Supporting Information, as explained below.

### 2.1 Inter-ionic potential and simulation details

In this work we used the inter-ionic potential developed by Thomas et al<sup>49</sup>. This potential was parameterized with reference to both experimental and first-principles data. It was shown to successfully reproduce the structural properties of  $\text{SrTiO}_3$  and  $\text{Sr}_3\text{Ti}_2\text{O}_7$ <sup>49,50</sup>, the bulk diffusion of oxide-ions<sup>51</sup> and the stacking fault energy and  $\langle 110 \rangle \{110\}$  dislocation structure of  $\text{SrTiO}_3$ <sup>52,53</sup>, as well as other properties.<sup>54,55</sup> This potential is a computationally-fast rigid ion model, consisting of a Born-Mayer part to describe the short range repulsion between ions and a Coulombic interaction. Partial charges are used which were derived from a Mulliken analysis of Density Functional Theory (DFT) data.<sup>49</sup> The parameters of this potential are also reported in Table S1 (Supporting Information).

The Thomas potential was originally parameterized for stoichiometric  $\text{SrTiO}_3$  only. The study of reduced  $\text{SrTiO}_{3-\delta}$  requires extra information on how to change the charge of Ti (and possibly also O and Sr) when this material is reduced. In previous work, Schie et al. have distributed the extra charge (resulting from the creation of oxygen vacancies) equally among all the Ti and O atoms.<sup>51</sup> In this paper, we use a similar approach and modify the Ti and O charges ( $q_{\text{Ti}}$  and  $q_{\text{O}}$ ), but with three times more charge assigned to each Ti cation than to each O anion, in accord with chemical intuition.<sup>42,43</sup> The charge distribution is calculated by the following equations:

$$q_{\text{Ti}} = 2.36 - \frac{Q}{2n_{\text{Ti}}} \quad (2a)$$

$$q_0 = -1.40 - \frac{Q}{2n_0} \quad (2b)$$

where  $Q$  is the total extra charge (e.g. 1.4 if one oxygen vacancy is introduced) and  $n_{\text{Ti}}$  and  $n_{\text{O}}$  are the number of Ti and O ions present in the system. We find that this yields a much better agreement with DFT calculations of the chemical expansion<sup>57</sup> and with the dependence of vacancy formation energy on lattice strain in SrTiO<sub>3</sub> (see Figures S1-3). Finally, we note that the charges assigned according to equations 2 are independent of the atom location.

We use the LAMMPS code to run Molecular Dynamics (MD) simulations at finite temperatures, as well as static relaxations at 0 K.<sup>58</sup> The simulated model with the dislocation will be reported in the section 2.2. We simulate bulk SrTiO<sub>3</sub> with 20×20×20 unit cell system (~40,000 atoms) with no dislocations. We dub this system “dislocation-free bulk SrTiO<sub>3</sub>” and use it as a reference throughout the paper. The dislocation-free bulk SrTiO<sub>3</sub> model is equilibrated in the NPT ensemble; longer runs (~ 5ns) are then performed in the NVT ensemble. In all calculations, long-range Coulombic interactions are summed using the PPPM method<sup>59</sup>, as implemented in LAMMPS; the short-range part of the potential is calculated within a cut-off distance of 12 Å. Diffusion coefficients are extracted from the slope of the mean squared displacement (MSD) of the ionic species of interest, as done in previous work.<sup>22,60–64</sup> Select migration barriers are calculated using the Nudged Elastic Band (NEB) method, as implemented in LAMMPS. We used between 5 and 10 images, depending on the migration pathway.

## 2.2 Dislocation set-up

The study of dislocations by means of atomistic simulations is complicated by their non-periodic nature and large spatial extent. These two challenges are overcome in this study by simulating two non-interacting dislocations with opposite Burgers vectors, ±<100> on the {110} slip plane, and by employing computationally efficient (though accurate) rigid-ion models, that allow us to simulate ~160,000 for sufficiently long time-scales (~ 30 ns). We note here that our approach allows us to focus on the role of a single dislocation, rather than a low-angle grain boundary with a periodic array of closely-spaced dislocations, as studied in ref.<sup>20</sup> Furthermore, using LAMMPS, a massively parallelized software, allows us to model the dislocation system at suitably large spatial and temporal scales.<sup>20</sup>

Two opposite <100>{011} edge dislocations are introduced in the simulation model as shown in Figure 1. The perovskite lattice structure is rotated to construct the x, y and z-axes of the simulation model along the <0̄1>, <100> and <011> crystallographic directions. These correspond to the dislocation line vector, Burgers vector and slip plane normal, respectively. We introduce a cut in the middle of the box by

removing two crystallographic planes (corresponding to a SrO and a TiO<sub>2</sub> plane), as shown in Figure 1a. The cut is healed by structural optimization, and forms two edge dislocations at the upper and lower parts of the simulation box. The upper dislocation has a Burgers vector of  $<100>$  and the bottom  $<\bar{1}00>$

It is important to note that, when the crystal is cut as shown in Figure 1a, the surfaces exposed at the two ends of the cut (that later make the dislocation core) are polar. This is because the cut surfaces at the top and bottom are {011} planes, which consist of alternating (SrTiO<sub>4</sub>)<sup>2-</sup> and (SrTiO<sub>2</sub>)<sup>2+</sup> layers. If nothing is done to counter this effect, one obtains two charged dislocations, a configuration that we found to be highly unstable. This instability stems from the large dipole that the two charged dislocation cores introduced into the system. The solution to this problem, depicted in Figure 1, is to simply move two of the extra oxygen ions in the top cut (corresponding to 50% of the total number of oxygen ions in that column) to the bottom cut, thus yielding two reconstructed, non-polar surfaces. This procedure forms two *identical* dislocation cores. The energy of the system is lowered by ~20 eV, confirming the validity of this approach in stabilizing the dislocation system. Furthermore, the dislocation structure is in agreement with that deduced from High Resolution-Transmission Electron Microscopy (HR-TEM) experiments<sup>65</sup> (see below). MD runs on this system maintain a stable dislocation configuration, as will be shown below.

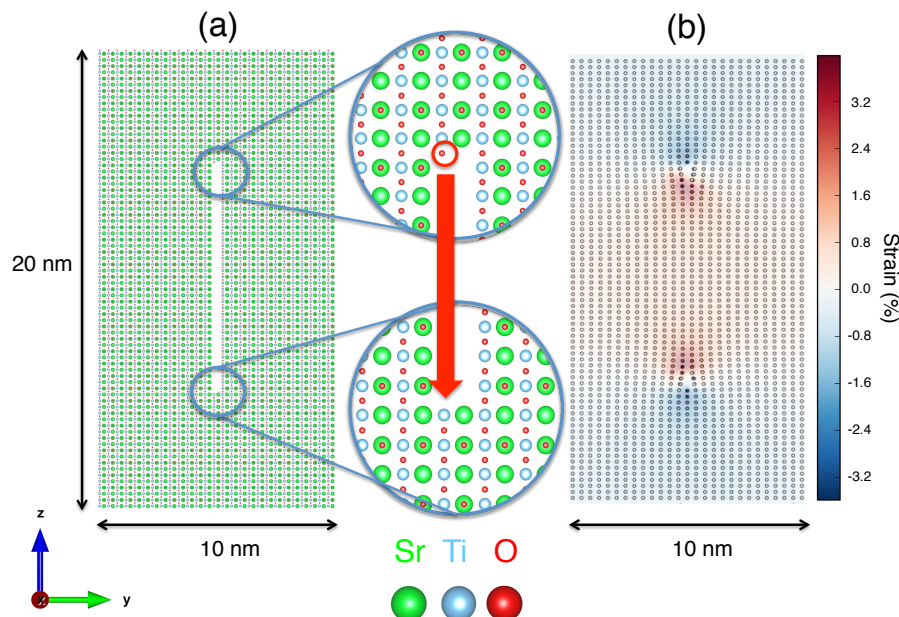


Figure 1: (a) Schematic of the procedure used to construct two opposite dislocations. First the box is rotated so that the x, y and z axes correspond to the  $<0\bar{1}1>$ ,  $<100>$  and  $<011>$  crystallographic directions. A cut is then introduced in the middle of the box by removing an SrO and a TiO<sub>2</sub> plane. To avoid having charged dislocation cores, half the oxygen atoms are moved from one core (top) to the other (bottom) shown by the red circle and arrow, to ensure that both surfaces are non-polar. The system is then relaxed, the cut heals and two identical dislocations are created. (b) Strain map for the equilibrated system, obtained by

1  
2  
3 calculating the local changes in the cation separation distances,  $\Delta d_{Sr-Sr} = (d_{dist}-d_{bulk})/d_{bulk}$ , where  $d_{dist}$  and  $d_{bulk}$  are the Sr-Sr bond  
4 distances in the model with a dislocation and in the unstrained dislocation-free bulk model, respectively, as done in previous  
5 work.<sup>22</sup> Circles in (b) are the Sr atom positions, while Ti and O are not shown for the sake of clarity. Tensile (red) and  
6 compressive (blue) zones can be observed, especially in the vicinity of the dislocations.  
7  
8  
9  
10

11 Figure 1b shows the strain map in the relaxed system, obtained by calculating local changes in the lattice  
12 parameter (see caption for further information). As expected, we observe zones in the vicinity of the  
13 dislocation cores with high tensile and compressive strains. The spatial extent of these zones is quite  
14 small, within 1 nm, in good agreement with experimental observations.<sup>6</sup> For larger distances from the  
15 cores, the system exhibits a homogeneous uniaxial strain along the y-axis (tensile in the middle of the slab,  
16 compressive in the upper and lower parts of the slab). This is because of the way the dislocations have  
17 been introduced. Since two atomic planes have been removed in the middle (see Figure 1a) and we use  
18 periodic boundary conditions, the system is uniaxially strained along the y-axis ( $<100>$ ) by +/- 2%. For  
19 large distances from the cores, the material can be assumed to behave as bulk (though uniaxially strained),  
20 i.e. it is not affected by the dislocation core or its local strain field.  
21  
22

23 The dimensions of the simulation box in Figure 1 are approximately 2 nm × 10 nm × 20 nm  
24 (corresponding to ~ 40,000 atoms). This means that the dislocation cores are separated by ~ 10 nm along  
25 z-axis ( $<011>$  direction), which we find to be sufficient to treat each dislocation as independent (see strain  
26 map in Figure 1b, and also the results below). The vacancy formation energy is converged at this size of  
27 the simulation model, which was proven by comparing with larger systems. When performing MD  
28 calculations for local diffusion coefficients, larger systems, 8 nm × 10 nm × 20 nm (160,000 atoms), are  
29 simulated to obtain better statistics. The diffusion coefficients were averaged over up to 5 independent  
30 simulations for those cases in which the diffusion was slow (see section 3.3.1).  
31  
32  
33  
34  
35  
36  
37  
38  
39  
40  
41  
42  
43  
44

### 45 3. Results

#### 46 3.1 Validation of the dislocation model in SrTiO<sub>3</sub>

47 Previous work has already shown that the Thomas potential for SrTiO<sub>3</sub> can accurately describe both the  
48 bulk structural and conducting properties<sup>49–51</sup> of SrTiO<sub>3</sub>, and the core structure<sup>52,53</sup> of the  $<110>\{110\}$   
49 edge and screw dislocations. Here we focus on the  $<100>\{110\}$  edge dislocation, which structure has  
50 been experimentally characterized in the literature.<sup>2,12,65</sup> In Figure 2, we report the simulated core  
51 structure. We remind the reader that both dislocations are identical by construction, so our description  
52 applies to either core. The dislocation core has a characteristic trapezoidal shape (highlighted by a yellow  
53  
54  
55  
56  
57  
58  
59  
60

trapezoid). The  $\text{TiO}_2$  plane at the core splits into half-filled columns of Ti and O (indicated by the top arrow splitting into two arrows), thus matching the structural pattern in the compressive zone. The split O columns at the top part (highlighted by a red rectangle in Figure 2b) have only two oxygen atoms out of four. The O columns at the bottom are both missing one oxygen atom out of four (highlighted by a red rectangle in Figure 2b). These missing oxygen atoms therefore constitute structural vacancies, at 50% and 25% in the top and bottom part of the core, i.e. they are present even if the  $\text{SrTiO}_3$  model, as a whole, is stoichiometric and their importance will be highlighted in section 3.3.

Comparison of our simulated core structure of the  $<100>\{011\}$  edge dislocation in  $\text{SrTiO}_3$  with the HR-TEM data of Jia et al (see Figure 3 of ref.<sup>65</sup>) shows that the simulated structure contains all the salient features of the experimentally imaged dislocation; i.e. the trapezoidal shape of the core, the splitting of  $\text{TiO}_2$  planes and the reduced occupancy of these columns because of their splitting at the dislocation core. The experimental diagram shows a slightly more disordered structure than the simulated one, e.g. some oxygen columns split into four columns at the core. This is probably due to the fact that we are starting with an ideal stoichiometric system during the construction of the model, as shown in Figure 2, while the structure in ref.<sup>65</sup> might contain impurities and oxygen vacancies.<sup>65,66</sup> We also note that some atomic columns in ref.<sup>65</sup>, especially in the case of Sr, have reduced occupancy, while we do not observe this feature in the simulated stoichiometric model. Again, this might be due to local changes in the material's composition and stoichiometry, though the authors also suggest that it might be due to limitations of the experimental technique.<sup>65</sup>

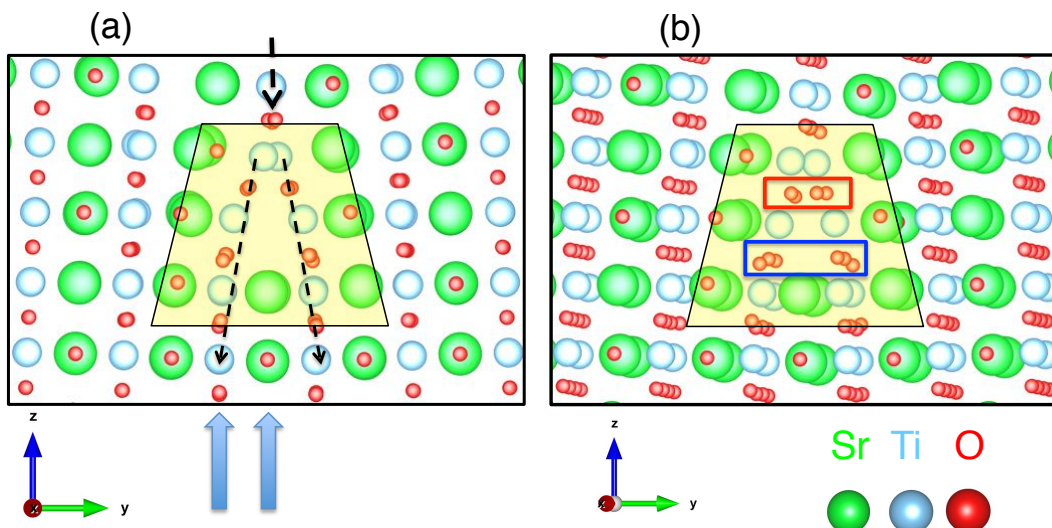


Figure 2: Dislocation core structure obtained from the static relaxation calculation. (a) is front view with the x-axis perpendicular to the screen direction while (b) is the same structure rotated around z, for showing the structural vacancies on the oxygen columns at the dislocation core. The large blue arrows from the bottom in (a) point to the  $\text{SrO}$  and  $\text{TiO}_2$  planes that

have been removed on the top part of the image to create the dislocation. Dashed arrows from the top are a guide to the eye for the splitting of the Ti and O columns, as discussed in the text. The red and blue rectangles in (b) indicate the O columns that have reduced occupancy, with 50% and 25% of structural oxygen vacancies per column, respectively.

In summary, the validated structure of the  $<100>\{011\}$  edge dislocation core in SrTiO<sub>3</sub>, together with the extensive validation of the Thomas potential performed by other groups,<sup>49–56</sup> makes us confident that this inter-ionic potential is suitable to assess the defect chemistry and transport properties along the dislocation in SrTiO<sub>3</sub>. We have performed further tests of the accuracy of this potential for bulk ionic conductivity, chemical expansion and vacancy formation energies of SrTiO<sub>3</sub>, which can be found in section 1 in the Supporting Information.

### 3.2 Effects of the $<100>\{011\}$ edge dislocation on the defect chemistry

In this section we assess the defect chemistry in the vicinity of the  $<100>\{011\}$  dislocation in SrTiO<sub>3</sub>. SrTiO<sub>3</sub> crystallizes in the densely packed perovskite structure, so the only type of point defects found in this material is vacancies on all three sublattices.<sup>12,67</sup> Here we focus on oxygen vacancies only, because they are relevant to the goal of this paper, and are energetically the most favored type of point defect under most conditions.<sup>68</sup>

Our calculations show that *the oxygen vacancy formation energy near the dislocation core is significantly lower than in dislocation-free bulk SrTiO<sub>3</sub>*, in the regime where the concentration of oxygen vacancies is low (ppm level). This can be seen in Figure 3, where we map the formation energy of a single oxygen vacancy (corresponding to a concentration of 0.004%) in the SrTiO<sub>3</sub> model with two edge dislocations. In this map we show only the oxygen ions (Sr and Ti cations are hidden for simplicity) and we color-code these ions according to the change in their vacancy formation energy,  $\Delta E_f^V$ , with respect to  $E_f^V$  obtained for bulk dislocation-free SrTiO<sub>3</sub>, similar to the approach used by Uberuaga and Benedek<sup>54</sup>.

Figure 3a shows our entire simulation box; most of the oxygen atom sites are white/grey, meaning that the energy required to remove them is similar to that in bulk SrTiO<sub>3</sub>. A closer look at these atoms (away from the dislocations) shows that their formation energy is actually slightly higher/lower in the compressive/tensile uniaxially strained parts of the model compared to bulk dislocation-free SrTiO<sub>3</sub>, the difference being small, ~ 0.2 eV. Lattice strain has been shown to affect the vacancy formation energy of several metal-oxide materials,<sup>69,70</sup> with tensile/compressive strain favoring/hindering vacancy formation (see also Figure S3). This factor explains the relatively small difference (~ 0.2 eV) in the formation energy of oxygen vacancies away from the dislocation core. On the other hand, the formation energy of oxygen vacancies close to the dislocation core (Figure 3b) varies significantly from the bulk value. Indeed, most of the oxygen sites at the dislocation core (highlighted by the black trapezoid) have vacancy

formation energies that are up to 2.0 eV lower than in bulk. Conversely, some of the oxygen sites in the compressive part of the dislocation, next to the core, have higher vacancy formation energies (up to 1.5 eV higher than bulk). Our results are in good agreement with the evidence from Electron Energy Loss Spectroscopy (EELS) measurements that have shown that  $\text{SrTiO}_3$  is oxygen deficient at the dislocation core,<sup>2,12,65,66</sup> and with previous calculations on  $\text{MgO}$ <sup>71</sup> and  $\text{SrTiO}_3$ .<sup>20</sup> The changes in the formation energy for oxygen vacancies at the dislocation core can be explained in terms of the local coordination environment of the oxygen ions. The oxygen ions at the dislocation core are under-coordinated – many have a coordination number of only 3, i.e. half of the coordination expected in bulk  $\text{SrTiO}_3$  (see Figure 2c). This under-coordination (i.e. the fact that there are fewer bonds to break) lowers the oxygen vacancy formation energy for these positions. This is conceptually similar to the behavior of oxide ions at the surface and/or grain boundaries, where the oxygen vacancy formation energy is also found to be lower.<sup>54,72–76</sup>

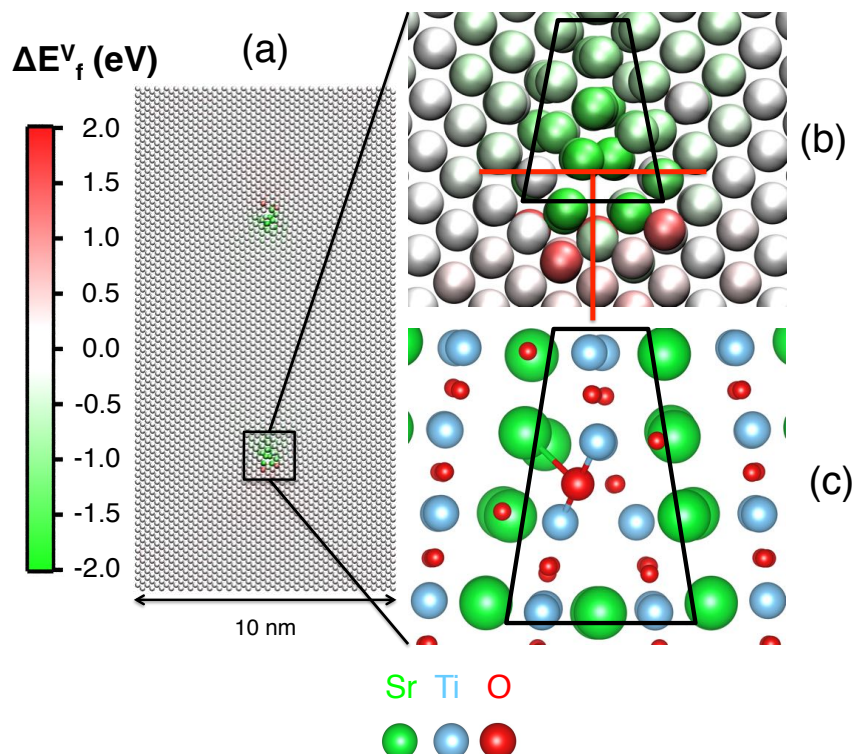


Figure 3: (a) Map of the change in the formation energy of oxygen vacancies,  $\Delta E_f^V$ , for the  $\text{SrTiO}_3$  with two dislocations relative to  $E_f^V$  obtained for bulk dislocation-free  $\text{SrTiO}_3$ . Only the oxygen atoms are shown and these are color coded according to  $\Delta E_f^V$ . (b)  $\Delta E_f^V$  map for one of the dislocation cores shown more closely. Oxygen atoms in the vicinity of the core have significantly lower vacancy formation energies (shown by green). (c) Atomic structure of the dislocation core. Each oxygen atom at the core is coordinated to only 3 cations, while the oxygen coordination in bulk  $\text{SrTiO}_3$  is 6. Green, azure and red spheres are  $\text{Sr}$ ,  $\text{Ti}$  and  $\text{O}$  atoms, respectively.

Figure 3b shows that it is energetically favorable to create one oxygen vacancy at the core of stoichiometric  $\text{SrTiO}_3$ . Next, we focus our attention on how many vacancies can actually be accommodated in this dislocation, i.e. how the vacancy formation energy changes with increasing amount of oxygen vacancies at the core. We find that *a maximum of 3 oxygen vacancies (for this size of the model) can be created at the core before the bulk starts reducing*, which corresponds to a vacancy concentration of  $\sim 8.0\%$  at the core. To estimate this, we proceeded as follows. We removed from each core one oxygen atom at the site with the lowest vacancy formation energy, that is shown in Figure 3. We then recalculated the formation energy map for this slightly oxygen-deficient system. Figure 4b shows that it is still favorable to create the next oxygen vacancy at the core. The reduction in vacancy formation energy, with respect to bulk, is 1.3-1.6 eV (in the previous case it was  $\sim 2.0$  eV). We repeated this procedure till we found that removing oxygen atoms from the core is no longer energetically favorable compared to bulk (i.e. away from the dislocations). We found that no more than 3 vacancies per core can be created (Figure 4d) in our system. We define the core as a circle of radius 0.4 nm i.e. about one unit cell lattice parameter of  $\text{SrTiO}_3$  (see Figure 4a). There are 37 oxygen atom sites in this region, which means that 3 vacancies correspond to 8.0% vacancy concentration at the core. This result can be interpreted as follows: if one starts reducing this material by slowly lowering the  $\text{pO}_2$  while equilibrating the system, one would reach a vacancy concentration of 8.0 % at the dislocation core before the bulk of the material starts reducing. Supporting section 4 reports an estimate of how many vacancies can be accommodated at the dislocation cores of a  $\text{SrTiO}_3$  sample as a function of the dislocation density. We stress that our calculation of concentration is based on formation energies only and neglects any entropic or phonon contributions or kinetic effects.

We note that the formation energy maps deduced here impact the first term, that is the concentration term, in Equation 1 for the diffusion coefficient. We note that space-charge effects have been invoked in the interpretation of oxide ion and electronic conductivity studies in  $\text{SrTiO}_3$ .<sup>20,75,77,78</sup> Here we assess the formation of a space-charge zone around the dislocation based on the formation energy of oxygen vacancies. In Figure 5a, we show the relative formation energy map of an oxygen vacancy in the  $\text{SrTiO}_3$  model with 3 vacancies per core. This is the same result as the one shown in Figure 4d, though the color scale and lateral size have been changed for clarity. The presence of oxygen vacancies at the dislocation core causes a depletion zone for oxygen vacancies around the dislocation (red/white region). In this depletion zone, which extends to a few nanometers (3-5 nm), the creation of a new vacancy costs at least 0.3 eV more than in the bulk away from the dislocation. From the data in Figure 5a, one can extract the expected vacancy concentration distribution using the following formula:

$$[V_O^{\bullet\bullet}] = [V_O^{\bullet\bullet}]_0 \exp[-(\Delta E_f^V)/k_B T], \quad (3)$$

where  $[V_O^{\bullet\bullet}]_0$  is the bulk vacancy concentration, corresponding to  $1.27 \times 10^{19} \text{ cm}^{-3}$  (6 vacancies in a model size of  $22.1 \text{ \AA} \times 105.6 \text{ \AA} \times 204.6 \text{ \AA}$ ) for the system in Figure 5a. This vacancy concentration profile is shown in Figure 5b as a function of distance from the dislocation core at 1000 K. As expected, a strong vacancy depletion is observed in the vicinity of the core, and the bulk vacancy concentration is only recovered 4-5 nm from the core. We note that the presence of two bands at slightly larger and smaller values than  $[V_O^{\bullet\bullet}]_0$  is due to the slightly different formation energy in the uniaxially tensile and compressive strained regions away from the dislocation core, respectively (see also caption of Figure 5). The space-charge profile of Figure 5b can be explained as follows. Positively charged oxygen vacancies accumulate at the core, because its under-coordinated structure makes it energetically easier to create vacancies. However, this accumulation of vacancies imparts a net positive charge at the core, and electrostatically repels other positively charged oxygen vacancies in the neighboring region. In effect, this is the formation of a space-charge zone around the dislocation, predicted and visualized from the atomistic scale, when the only charged defect is oxygen vacancy in  $\text{SrTiO}_3$ , where the electrons are treated to be totally delocalized over all the Ti and O ions (see section 2). We also note that the quantitative result in Figure 5 is valid for the given concentration of oxygen vacancies, and one should expect a different result depending on the concentration, for example a weaker space-charge zone with increasing concentration of oxygen vacancies.

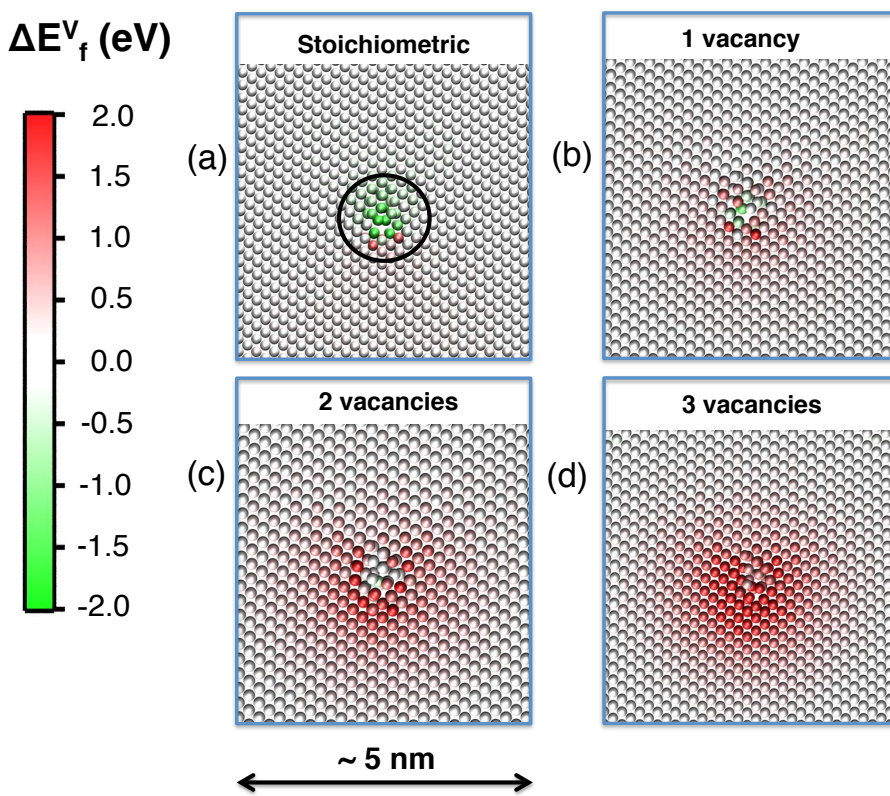


Figure 4: Relative formation energy  $\Delta E_f^V$  maps of a single oxygen vacancy in stoichiometric  $\text{SrTiO}_3$  (a), in  $\text{SrTiO}_3$  with 1 vacancy per core (b), in  $\text{SrTiO}_3$  with 2 vacancies per core (c), and in  $\text{SrTiO}_3$  with 3 vacancies per core (d). The lowest formation energy in each model is lower than the bulk value by 2.0, 1.6, 0.8 eV in (a), (b) and (c), respectively. The circle in (a) has a radius of 0.4 nm (see also text).

A similar behavior to that reported in Figure 5 has been observed experimentally by De Souza et al. at the surface of  $\text{SrTiO}_3$ .<sup>20,75,77</sup> By performing  $^{18}\text{O}$  exchange and tracer diffusion experiments, the authors have found evidence of vacancy depletion near the surface of  $\text{SrTiO}_3$ ; this layer extends over 5-30 nm beneath the surface, depending on several experimental factors, such as the surface termination and morphology. This value appears larger than the spatial extent predicted in Figure 4e. One reason for this difference is that the employed potential significantly underestimates the dielectric constant of  $\text{SrTiO}_3$  in this work (a well-known and unavoidable shortcoming of rigid-ion potentials<sup>49</sup>). Knowing that the space-charge length is proportional to the square root of the dielectric constant,<sup>77,79</sup> one can rescale our predicted spatial extent of the charge separation by  $\sqrt{\epsilon_{\text{exp}}/\epsilon_{\text{calc}}} = 7.9$ , where  $\epsilon_{\text{exp}}$  and  $\epsilon_{\text{calc}}$  are the experimental and calculated dielectric constants, respectively (see Supporting Section 1.5). This scaling increases our predicted depletion region from 4-5 nm to 32-40 nm, which is in good agreement with the experimental results of

De Souza et al.<sup>75</sup>, and with the range 32-56 nm calculated by using eq. 23 of ref. <sup>77</sup> (here we used the experimental dielectric constant, 300, and a space-charge potential in the 0.4 - 0.8 eV range, in agreement with refs. <sup>20,75</sup>). Finally, we point out that the presence of such a heterogeneous concentration profile of vacancies can have a significant effect on the electrical (ionic and electronic) conductivity<sup>20,75</sup> of this material (see equation 1), a point that will be discussed in the next sections.

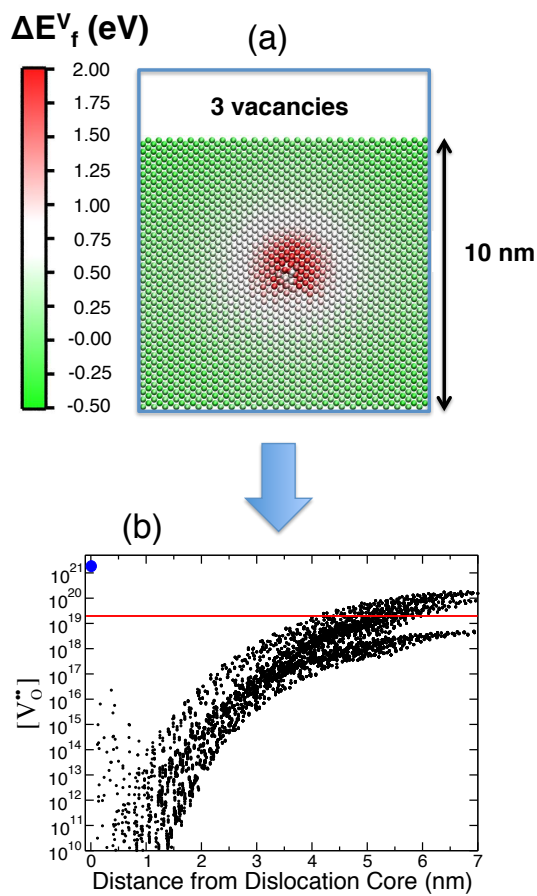


Figure 5: (a) Relative formation energy  $\Delta E_f^V$  for the same model reported in Figure 4d, but with a different color scale (between -0.5 and 2.0 eV) and larger lateral size, to more clearly see the extent of the space-charge region around a non-stoichiometric dislocation core. (b) Vacancy concentration vs. distance from the dislocation core, as calculated from equation 3 at 1000 K. The red horizontal line indicates the bulk concentration,  $[V_0^*]_0 = 1.27 \times 10^{19} \text{ cm}^{-3}$  (assuming the vacancies in the entire model are randomly distributed, as a reference value), while the blue circle at 0 nm indicates the vacancy concentration in the vicinity of the core (3 vacancies, see Figure 4), corresponding to  $3.94 \times 10^{21} \text{ cm}^{-3}$ . We note that, because of the uniaxial tensile and compressive strain present in regions away from the dislocation (see Figure 1), the formation energy in these regions is slightly larger or smaller than in the unstrained bulk SrTiO<sub>3</sub>, respectively (see Figure 3 and following discussion). For this reason  $[V_0^*]$  away from the dislocation shows two bands that plateau at higher and lower values than  $[V_0^*]_0$  in the uniaxially tensile and compressively strained zones of the simulation model, respectively.

### 3.3 Effects of the $\langle 100 \rangle\{011\}$ edge dislocation on the oxide-ion conductivity

We now turn our attention to the effect of dislocations on the oxide-ion conductivity in SrTiO<sub>3</sub>. We study two different regimes of vacancy concentration. The first one is a low vacancy concentration (dilute) regime, with an overall vacancy concentration of 0.017 %, corresponding to approximately 200 ppm. This is equivalent to having fewer vacancies than the maximum number that is favorable to form at the dislocation core compared to the bulk (see Figure 4). This dilute regime is relevant to resistive-switching applications of SrTiO<sub>3</sub>. The second regime has a significantly higher vacancy concentration, in the range of 0.5-2.5 %. In this case, the total number of vacancies is several orders of magnitude higher than what can be accommodated favorably at the dislocation core that was shown in Figure 4. We note here that such high vacancy concentrations can only be achieved at high temperatures and low  $pO_2$ , or by doping, and are therefore more relevant to applications such as fuel cells, separation membranes, catalysis or sensors.

#### 3.3.1 Low vacancy concentration regime (~200 ppm)

In the low vacancy concentration regime (0.017%), we assess two different cases. In the first case (sample I), the starting configuration is taken from Figure 4c, i.e. vacancies are already in their most stable position at the dislocation core. In the second case (sample II), the vacancies are randomly distributed in the material. In principle, these two cases should yield identical results because the vacancy distribution in sample II should equilibrate to the lowest energy configuration predicted in Figure 4, unless kinetic effects play a role in the limited time-scale of MD simulations, as discussed later.

Figure 6a shows the different regions of the SrTiO<sub>3</sub> simulation model from which we extract diffusion coefficients. These are the one-dimensional diffusion coefficients along the dislocation (denoted as  $D_x$ ), which allows us to assess whether there is fast pipe diffusion. Our calculations show that the diffusion coefficients along the other directions ( $D_y$  and  $D_z$ ) are smaller than that of the bulk, as recently also observed in our recent work on ceria.<sup>22</sup> The computed diffusivity along the dislocation,  $D_x$ , is normalized by the one-dimensional diffusivity in the bulk dislocation-free SrTiO<sub>3</sub> model, with the same concentration of oxygen vacancies and at the same temperature.

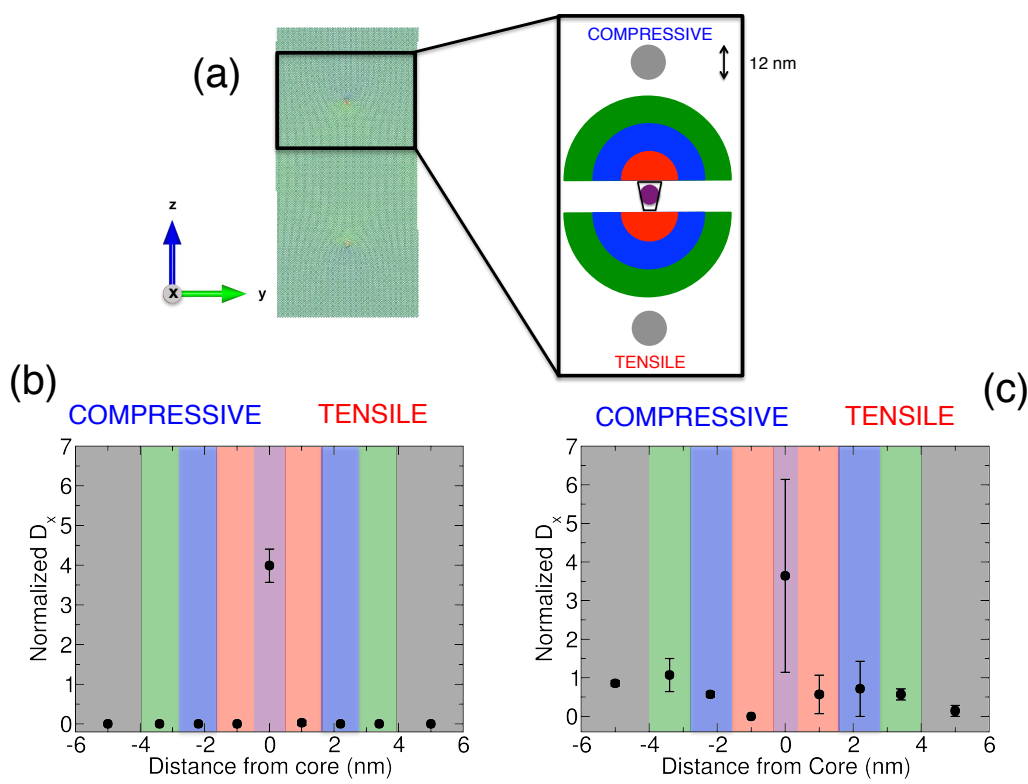


Figure 6. (a) Schematic of the different regions used for the calculation of the local diffusion coefficients in  $\text{SrTiO}_3$  along the dislocation line. The dislocation core is shown as a black trapezoid. We define one cylindrical region (purple) of radius 0.4 nm as the dislocation core. We then define 6 semi-cylindrical regions, 3 in the tensile (red/blue/green bottom regions) and 3 in the compressive (red/blue/green top regions) parts of the simulation model. Finally, two bulk regions are defined (grey cylinders) 5 nm away from the dislocation, one in the uniaxial tensile and one in the uniaxial compressive part. Normalized  $D_x$  in sample I (b) and sample II (c) vs. average distance from the core are plotted for different regions shown in (a). The data was obtained by averaging over 5 independent calculations for sample I and 3 for sample II. Error bars are the standard deviation from the different runs and in most cases are smaller than the symbol size. In both plots  $D_x$  is normalized by the one-dimensional diffusivity in the bulk dislocation-free  $\text{SrTiO}_3$  model and the total vacancy concentration is 0.017%. The simulations were performed at 1200 K and were 20-30 ns long.

Our results show that the diffusion coefficient varies significantly from one region to another for sample I, in which the starting vacancy distribution is taken from that in Figure 4c. This is shown in Figure 6b that reports the normalized  $D_x$  at 1200 K, plotted versus the average distance of the studied region with respect to the dislocation core. Negative/positive distances are used to indicate the compressive/tensile parts of the model. First, we note that most of the calculated diffusion coefficients in sample I are equal to zero, within the statistical error. The only diffusion coefficients that are non-zero are either in the dislocation core region or in the tensile region next to the dislocation core (the latter being very small, see Table 1). Analysis of the vacancy positions (see Supporting Figure 5) reveals that vacancies reside in the vicinity of

the dislocation cores and never move away from them during the 30 ns of MD simulation. This is consistent with the findings summarized in Figure 4, which shows that there is a significant energy gain for vacancies to be at the dislocation core. Second, we observe that the diffusion coefficient at the core of the dislocation is larger than that of dislocation-free bulk SrTiO<sub>3</sub>, by a factor of ~4.0, which is quite significant. While this might look like evidence for pipe-diffusion along the dislocation, below we demonstrate that this is not the case.

Table 1: Calculated diffusion coefficients in SrTiO<sub>3</sub> with 0.017% vacancy concentration in sample I (with an equilibrated distribution of vacancies) at 1200 K. We only report those values that are non-zero along the dislocation line, D<sub>x</sub>. Errors are estimated from the standard deviation of the values obtained from 5 and 2 independent calculations for sample I and for the stoichiometric SrTiO<sub>3</sub>, respectively. Values for the bulk diffusion coefficient, D, from a simulation of stoichiometric SrTiO<sub>3</sub> and from several experiments<sup>47,75,80</sup> are also reported.

Distance from core (nm)	D <sub>x</sub> or D (10 <sup>-10</sup> cm <sup>2</sup> /s)
-0.4 → 0.4	5.6 ± 0.6
0.4 → 1.6	0.04 ± 0.08
Core of stoichiometric SrTiO <sub>3</sub> (-0.4 → 0.4)	6.2 ± 4.8
Dislocation-free bulk SrTiO <sub>3</sub>	1.4 ± 0.0
Dislocation core (from ref. <sup>47</sup> at 1073 K)	0.1
Bulk (from ref. <sup>47</sup> at 1073 K)	10 <sup>-5</sup>
Bulk (from ref. <sup>75</sup> at 1073 K)	0.2
Bulk (from ref. <sup>80</sup> at 1073 K)	10

We now compare our results to the experimental data available in literature. Only the work of Szot et al.<sup>47</sup> provides an estimate of both the bulk and dislocation diffusion coefficients at 1073 K in SrTiO<sub>3</sub>, from an <sup>18</sup>O tracer diffusion experiment. Indeed, our calculated D<sub>x</sub> values for the dislocation are in the 5.6–0.04×10<sup>-10</sup> cm<sup>2</sup>/s range at 1200 K (see Table 1), which is in reasonable agreement with Szot's finding of 0.1×10<sup>-10</sup> cm<sup>2</sup>/s (considering our calculations are at a higher temperature by 127 K). Table 1 also reports the experimental values from various reports for the bulk diffusion coefficient of SrTiO<sub>3</sub>, but these span 6 orders of magnitude, thus making a comparison hard.

In order to pin down the origin of the higher diffusion coefficient at the dislocation core, we consider two possible factors, as described in Equation 1. First is increased mobility, which should be reflected by lower migration energies. Second is increased vacancy concentration, as noted above and in Figure 4. We performed static NEB calculations to estimate the migration barrier of an oxygen ion diffusing along the dislocation. These barriers have been calculated by introducing one oxygen vacancy in either column 1, 2 or 3 (see Figure 7), and then calculating the energy barrier for a neighboring oxygen atom to migrate to this vacant site. These jumps were found to have different migration barriers depending on the vacancy

position along the column because of the asymmetric environment around the dislocation. We therefore surveyed all these migration pathways and report only the highest barrier measured per each column along the dislocation (Table 2). We note that, since oxide ion diffusion involves a series of consecutive hops of an oxide ion along the column, the hop with the highest energy barrier is the rate-limiting step for diffusion along the dislocation.

Table 2: Migration barriers calculated from nudged elastic band calculations. For the sake of simplicity, we report here only the largest-barrier-path calculated along each column.  $E_{m,f}$ ,  $E_{m,b}$  and  $E_{ass}$  are the forward, backward and association energies for a given path, as explained in the text. Note that even though we're reporting the forward and backward migration barriers for each path, the diffusion will be limited by the higher barrier since equivalent paths are connected in series along the dislocation.

Column	$E_{m,f}$ (eV)	$E_{m,b}$ (eV)	$E_{ass}$ (eV)
1	1.02	0.0	1.02
2	2.05	0.15	1.9
3	2.00	0.90	1.1
Dislocation-free bulk	0.90	0.90	0.0

Our results (summarized in Table 2 and Figure 7) clearly show that the migration energies at the core are higher than in bulk  $\text{SrTiO}_3$ , so that the concept of pipe diffusion with a higher mobility for oxygen is not valid along the dislocation in  $\text{SrTiO}_3$ . As an example, in Figure 7 (b) and (c) we report the migration trajectory and the minimum energy path (MEP), respectively, of an oxygen ion diffusing along column 3. We note that the trajectory is curved, which is consistent with the well-known path shape for oxygen migration in perovskite oxides.<sup>81,82</sup> The MEP has two key features. First, the migration energy barrier (2.00 eV) is significantly higher than the value calculated in dislocation-free bulk  $\text{SrTiO}_3$  (0.90 eV). Second, the initial and final points have different energies, meaning that vacancies prefer to reside in, or are preferentially bound to, certain sites along the column. This preference is because different oxygen atoms in the same columns have different coordination environments (e.g. cation-oxygen bond distances change significantly from one site to another), making certain sites more favorable than others. The difference between the initial and final energy that represents the association energy is reported in the last column of Table 2. Such large association energies (up to 1.9 eV) increase the total migration energy and therefore hamper the oxygen diffusion, especially at lower temperatures, as observed in other ionic conductors.<sup>48,63,83</sup>

Next, we consider sample II, in which vacancies are randomly distributed at the start of the simulation. Like in the case of sample I, we observe the highest diffusion coefficient at the dislocation core. However, sample II also shows non-zero diffusion coefficients in several other regions, both in the compressive and tensile part, with no clear trend between the magnitude of the diffusion coefficient and distance from the core (see also section 3.3.2). An analysis of the vacancy positions explains this behavior. After 20 ns,

most vacancies are still randomly distributed in the material and have not moved to the dislocation core to equilibrate. Those regions that contain oxygen vacancies are the ones that show oxide-ion diffusivity. Sample II therefore seems to be in a metastable state in which vacancies have not reached their equilibrium distribution (that favors them to be all at the core, as in Figure 4 and sample I). In order to better understand the metastability of sample II, we estimate the average distance,  $l$ , travelled by a vacancy using the following formula:

$$l = \sqrt{D_v t} \quad (3),$$

where  $D_v$  is the vacancy diffusion coefficient (related to the oxygen diffusion coefficient via  $D_v \cdot [V_O^{''}] = D_o \cdot [O]$ ) and  $t$  is the time. Using the data from our calculations (reported in Table 3), we obtain  $l = 1.3$  nm on sample II for  $t = 20$  ns. This distance is not sufficient to achieve an equilibrium vacancy distribution in our large system (the average vacancy-vacancy distance is 5 nm). Furthermore, we note that because of the depletion zone around the core (red area in Figure 5a), the diffusion of vacancies into the core might be further hampered and therefore  $l$  might be significantly smaller than what we predict here (see also discussion on space-charge in previous section).

On the other hand, under typical experimental time-scales (1 hour) at room temperature,  $l$  is in the range of  $10^3$ - $10^5$  nm (again neglecting the effects of the vacancy depletion zone around the dislocation). This is significantly larger than the average dislocation-dislocation distance extracted from the data in ref. <sup>47</sup> ( $\sim 160$  nm) and is comparable to that of the annealed single crystal SrTiO<sub>3</sub> samples (1300 nm), as in ref. <sup>84</sup>. Therefore, under experimental conditions (i.e. dislocations introduced into the specimens, for example, by mechanical deformation, and kept at room temperature for extended periods), we expect the situation along dislocations to be closer to the case of sample I (equilibrated). But how many vacancies then remain in the bulk (zones away from the dislocation) depends on the dislocation density of the specimen, the vacancy concentration (see also section 4 in Supporting Information), the temperature and time and will affect the total bulk diffusion coefficient.

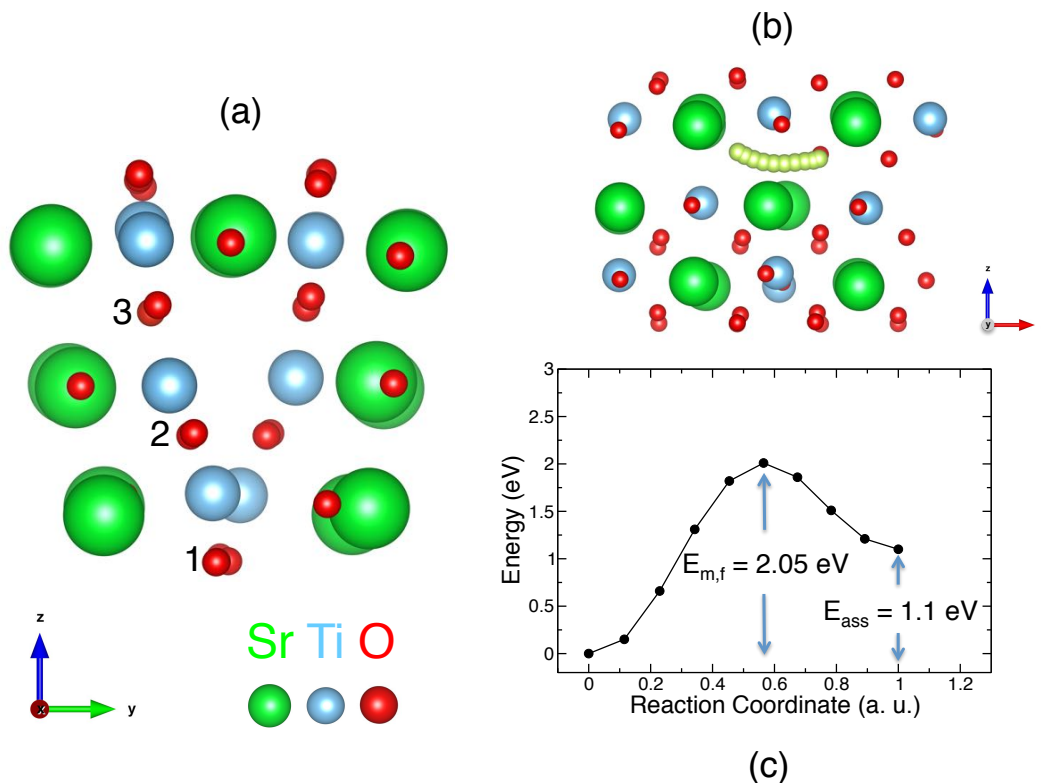


Figure 7: (a) Dislocation core structure in which we highlight the three oxygen columns used for the calculations summarized in Table 1. (b) Migration trajectory of one oxygen atom along column 3 (light yellow). Note that the image in (a) has been rotated around  $z$  in (b) to show the diffusion path along the  $x$ -axis (the dislocation line) in-plane. (c) Minimum energy path for the trajectory shown in (b), calculated by the nudged elastic band method.

A final interesting observation is that we find some oxide ion diffusion along the dislocation core even when SrTiO<sub>3</sub> is stoichiometric. Indeed, in when simulating fully stoichiometric SrTiO<sub>3</sub> (1200 K for 30 ns), we calculated a diffusion coefficient,  $D_x$ , of  $6.2 \times 10^{-10}$  cm<sup>2</sup>/s for the dislocation core (this value was obtained as an average over two independent calculations), a value of the same order of magnitude of that calculated along the dislocation of sample I (see Table 2). In all the other regions, no diffusion was observed because of lack of vacancies. Figure 2b provides an explanation for this otherwise unexpected result. Indeed, because of the way a dislocation is formed, some oxygen columns at the dislocation core have a reduced occupancy, even if the system is stoichiometric. These *structural* vacancies are therefore responsible for the observed oxide-ion diffusion at the dislocation core even when SrTiO<sub>3</sub> is fully stoichiometric. NEB calculations confirmed this finding by showing that oxygen migration through these structural vacancies is possible, though the migration energy is high (1.7 – 2.2 eV).

Table 3: Average distance,  $l$ , travelled by an oxygen vacancy in SrTiO<sub>3</sub> in our simulations and in an experiment at room temperature. We note that the experimental diffusion coefficients are obtained by extrapolating high-temperature data, as done in ref.<sup>37</sup>.

System	$D_O$ (10 <sup>-10</sup> cm <sup>2</sup> /s)	$D_V$ (10 <sup>-10</sup> cm <sup>2</sup> /s)	Time, $t$ (ns)	Distance, $l$ (nm)

<b>0.017% [V<sub>o</sub>"] @ 1200 K (MD simulation in this work)</b>	1.4	8400	20	1.3
<b>0.017% [V<sub>o</sub>"] @ 300 K (typical experimental conditions)</b>	$10^{-12}$ - $10^{-14}$ from refs. <sup>47,75,80</sup>	$10^{-9}$ - $10^{-11}$	$3.6 \times 10^{12}$	$10^3$ - $10^{-5}$
<b>2.5% [V<sub>o</sub>"] @ 1200 K (MD simulation in this work)</b>	14.7	588	20	0.34

In summary, the results in Figure 6 and Table 1 clearly show that the oxygen diffusion coefficient can be strongly heterogeneous in sample I. This is because, for low vacancy concentrations, SrTiO<sub>3</sub> tends to accumulate most of the vacancies in the vicinity of the dislocation cores (which show significant oxygen diffusion), while the remainder of the material is left stoichiometric (thus with no oxygen diffusion). A consequence of this is that dislocations are oxygen-deficient, as indeed observed in refs.<sup>2,12</sup>. The resulting oxygen diffusion coefficient along the dislocation is then higher than that in the dislocation-free bulk SrTiO<sub>3</sub> because of an increased oxygen vacancy concentration (i.e. [V<sub>o</sub>"] in Equation 1), and not because of an increased mobility (i.e.  $\exp(-E_m / k_B T)$  in Equation 1) at the dislocation.

### 3.3.2 High vacancy concentration regime (0.5% and 2.5%)

We now turn our attention to the role of dislocations on the oxide-ion mobility for SrTiO<sub>3</sub> with relatively high vacancy concentrations. Here we investigate SrTiO<sub>3</sub> with 0.5% and 2.5% vacancy concentration, respectively. This is a significantly higher concentration of oxygen vacancies than considered before and the number of vacancies considered here is a lot higher than what can be accommodated at the core, according to the results in Figure 4. So we expect the vacancy distribution to be relatively homogeneous and the resulting diffusion coefficients to behave differently from what we found above for the dilute regime.

In Figure 8 we show the normalized diffusion coefficient,  $D_x$ , for different zones of SrTiO<sub>3</sub> for 0.5% (a) and 2.5% (b) vacancy concentration, respectively. The behavior for the two vacancy concentrations is quite similar, so here we can make a series of general observations that are relevant to both plots. First, at large distances from the dislocation core, the material is uniaxially strained along the y-axis, as explained in section 2.2 and Figure 1. For this reason the diffusion coefficients in the tensile/compressive parts are higher/lower than in the bulk dislocation-free SrTiO<sub>3</sub>, resulting in normalized  $D_x$  values that are smaller/greater than 1. This is in good agreement with our calculation in bulk dislocation-free SrTiO<sub>3</sub> that

is uniaxially strained along the y-axis (see Table 4), and with recent work showing that other related oxides present a higher/lower diffusion coefficient when they are tensile/compressively strained<sup>22,85–89</sup>. In the tensile part of the model, as one moves closer to the core, the diffusion coefficient increases by as much as a factor of 3.5 (Figure 8b). The opposite happens in the compressive zone, where the diffusion coefficient decreases significantly as one approaches the core. Again, this is in agreement with the common understanding that compressive/tensile strain decreases/increases the oxide ion diffusivity.<sup>60,85–89</sup>

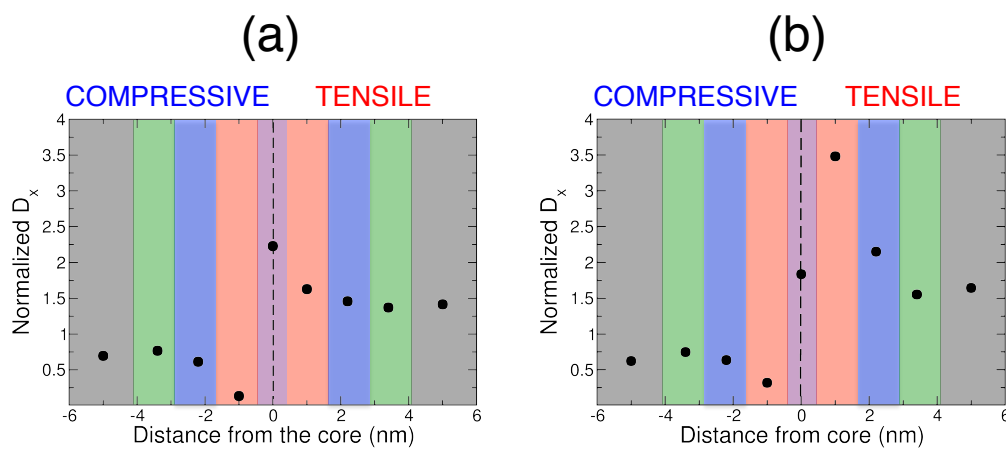


Figure 8: Calculated normalized diffusion coefficient along the direction of the dislocation line,  $D_x$ , as a function of average distance from the core for 0.5% vacancy concentration (a), and for 2.5% vacancy concentration (b). These calculations were performed at 1200 K and the simulations were run for 5–20 ns. See Figure 5(a) for the schematic of regions in which  $D_x$  was calculated.

Table 3 reports the values of the diffusion coefficients shown in Figure 8b. The tensile zones that are closest to the core exhibit diffusion coefficients that are higher than the value at 5 nm away from the core (grey area, right-hand side of Figure 8b). To quantify the spatial extent of the influence of a dislocation, we averaged the diffusion coefficient over a circular region around a dislocation. The values are reported in Table 4. One can see that as the radius of this region is increased (from 1.0 to 3.4 nm), the average diffusion coefficient decreases from  $27.5 \times 10^{-10}$  cm<sup>2</sup>/s to  $19.2 \times 10^{-10}$  cm<sup>2</sup>/s, the latter being already quite close to that of dislocation-free SrTiO<sub>3</sub> ( $14.7 \times 10^{-10}$  cm<sup>2</sup>/s, from MD simulations here). This means that, overall, the enhancement in the diffusion coefficient is limited to a very small region around the dislocation, and the enhancement itself is only within twice that of the bulk diffusivity.

Compared with the results shown in Figure 6, the main difference here is the more homogeneous character of the oxide-ion diffusivity. While in the dilute regime, SrTiO<sub>3</sub> with 0.017% vacancy concentration showed diffusion only at the dislocation core region, SrTiO<sub>3</sub> with higher vacancy concentrations have finite diffusion coefficients in all the regions as shown in Figure 8 and Table 4. This

is because the oxygen vacancy concentration studied here is  $100\times$  larger than that of sample I & II, which is significantly more than what can be accommodated at the core. The remaining vacancies are therefore free to distribute homogeneously in the system, which has been confirmed by performing a vacancy analysis (see Table S3). Using equation 3, we can calculate the average distance,  $l$  (0.34 nm), traveled by a vacancy during this simulation, as done before. While this is smaller than that for sample II (1.3 nm), the  $100\times$  larger vacancy concentration studied means that the vacancy-vacancy distance is significantly smaller. Indeed, one finds that there are enough vacancies within a distance  $l$  of the dislocation to completely saturate the core. We therefore conclude that the vacancy distribution of these heavily oxygen deficient compositions can be assumed to have reached equilibrium, unlike the case of sample II.

*Table 4: Oxygen diffusion coefficients along the dislocation line direction,  $D_x$ , at 1200 K and migration energies of 2.5% oxygen-deficient  $\text{SrTiO}_3$ , for the different zones as shown in Figure 5. The errors associated with the diffusion coefficients are usually  $\sim 5\%$ , while those associated with the migration energy barriers were estimated to be  $\sim 0.05$  eV (see section 2 of the Supporting Info for details). Migration energy barriers were calculated for runs between 1000 K and 1500 K.*

Distance from core (nm)	$D_x$ ( $10^{-10}$ cm $^2$ /s)	$E_m$ (eV)
<b>-5.6 → -4.4</b>	9.2	$0.99 \pm 0.05$
<b>-4.0 → -2.8</b>	11.0	$1.01 \pm 0.05$
<b>-2.8 → -1.6</b>	9.3	$1.0 \pm 0.05$
<b>-1.6 → -0.4</b>	4.7	$1.02 \pm 0.05$
<b>-0.4 → 0.4</b>	27.0	$0.87 \pm 0.05$
<b>0.4 → 1.6</b>	51.2	$0.77 \pm 0.05$
<b>1.6 → 2.8</b>	31.6	$0.87 \pm 0.05$
<b>2.8 → 4.0</b>	22.7	$0.92 \pm 0.05$
<b>4.4 → 5.6</b>	24.2	$0.92 \pm 0.05$
<b>Dislocation-free bulk</b>	14.7	$0.93 \pm 0.05$
<b>Average within 1.0 nm radius from dislocation core</b>	27.5	$0.82 \pm 0.05$
<b>Average within 2.2 nm radius from dislocation core</b>	22.3	$0.88 \pm 0.05$
<b>Average within 3.4 nm radius from dislocation core</b>	19.2	$0.91 \pm 0.05$
<b>Tensile uniaxial strained (2.5%) dislocation-free bulk</b>	18.9	$0.86 \pm 0.05$
<b>Compressive uniaxial strained (2.5%) dislocation-free bulk</b>	10.0	$1.01 \pm 0.05$

Finally, we note that we have surveyed a series of temperatures (from 900 to 1500 K) and we can confirm that in all cases the behavior is quite similar to that shown in Figure 8. In Table 3, we report the calculated migration energies for the different regions in  $\text{SrTiO}_3$  with a vacancy concentration of 2.5%. It can be seen that the tensile/compressive zones have migration energies that are lower/higher, consistent with the

diffusion coefficient data in Figure 6. The calculated migration energies in these two regions are similar to those extracted from calculations on bulk dislocation-free  $\text{SrTiO}_3$  strained along one axis by ~ 2%, which confirms the reliability of these values. The only regions that have migration energies lower than dislocation-free bulk  $\text{SrTiO}_3$  are those tensile regions close to the dislocations. The dislocation core itself (-0.4 → 0.4 nm in Table 4) has a migration energy that is essentially the same as that of dislocation-free bulk  $\text{SrTiO}_3$ . This result is different from the higher migration energies reported for the dislocation core in Table 2 for the dilute system. However, as the name implies, in this “high vacancy concentration” regime, significantly more vacancies are present in the model than those studied in Table 2 and Figure 7. The presence of several vacancies near the core can easily change the energy landscape (in particular the binding strength of certain sites at the core), as observed in Figure 4. In conclusion, based on the results in Table 4, we do not expect a significant enhancement of the oxide ion diffusion coefficient along the dislocation line even at lower temperatures. In other words, in this regime, too, pipe diffusion with enhanced mobility of oxygen ions is not present at the edge dislocation core in  $\text{SrTiO}_3$ .

#### 4. Discussion

The results obtained in this paper provide a thorough and atomistic understanding of the effects of an edge dislocation on the electrical and chemical properties of  $\text{SrTiO}_3$ . In this section we discuss the implications of our results for  $\text{SrTiO}_3$  performance in devices such as red-ox based resistive switching memories and SOFCs.

A key result of this work is that dislocation cores are more easily reduced compared to the bulk of the material. While similar observations have been made for grain boundaries and surfaces,<sup>20,54,72–76</sup> this is the first time this effect is demonstrated and quantified for isolated dislocations in  $\text{SrTiO}_3$ . We find that the main driving force is the under-coordination of the oxygen ions at the core, a feature that dislocations share with grain boundaries and surfaces. The predicted reducibility of the dislocation is in agreement with experimental evidence showing that  $\text{SrTiO}_3$  is oxygen-deficient in the vicinity of a dislocation core.<sup>2,12,65,66</sup>

The ease of reduction at dislocation cores in  $\text{SrTiO}_3$  has significant implications for the resistive switching behavior of this material. We note that the reducibility of the  $\text{SrTiO}_3$  at the dislocation impacts simply and directly the thermodynamics of defect chemistry in this material, and is not driven by faster migration or oxygen exchange kinetics along the dislocation. Indeed our result actually excludes faster migration, since our calculated migration barriers at the dislocation core are higher than that in bulk. Szot et al.<sup>2</sup> recently suggested that “the extended dislocation acts as (pipe) diffusion path allowing preferential exchange of oxygen with the surroundings.” It is true, as demonstrated also by Szot et al.<sup>2</sup> that the

1  
2  
3 electrical conductivity of this material under strong electric fields is determined by the electrical  
4 properties of dislocations. However, the dislocations induce local changes of electrical properties not  
5 because of the preferably faster kinetics of oxygen exchange or migration (pipe diffusion), but simply  
6 because of the structure-driven reducibility, i.e. a thermodynamic factor. The lower formation enthalpy of  
7 oxygen vacancies in the vicinity of a dislocation allows to reduce the SrTiO<sub>3</sub> preferentially along a  
8 dislocation under electric field. This reduced zone forms electronically conducting paths along the  
9 dislocation lines because of the compensating Ti *d* electrons released upon reduction,<sup>20,39,40,43</sup> while the  
10 bulk of SrTiO<sub>3</sub> remains in a stoichiometric insulating state, as hypothesized by Szot et al. Our finding in  
11 this work provides an atomistic clarification for the resistive switching mechanism along dislocation of  
12 SrTiO<sub>3</sub>, and helps to develop more accurate and quantitative models for switching kinetics. Finally, we  
13 note that, based on our results, we expect other extended defects, e.g. grain boundaries, to play a similar  
14 role in resistive switching in SrTiO<sub>3</sub>, since these also show lower oxygen vacancy formation energies.<sup>54,76</sup>  
15  
16

17 Another consequence of the ease of reduction at dislocation cores is the formation of a space-charge zone.  
18 As shown in Figure 5b, we were able to construct and visualize, from the atomic level, the space-charge  
19 zone around a reduced dislocation core (in the case of 8% vacancies at dislocation core) by using the  
20 calculated formation energies shown in Figure 5a. We note the atomistic calculations here take into  
21 account both the elastic strain field around the dislocation *and* the electrostatic interaction between the  
22 positively charged core and the positively charged oxygen vacancies mapped around the core. In fact, it  
23 appears from Figures 5 that the electrostatic repulsion effect dominates as there is only negligible  
24 difference in the relative formation energies of oxygen vacancies between the tensile and compressive  
25 strain fields of the dislocation. These two contributions together correspond to solving the Poisson  
26 equation with an electrostatic boundary condition at an extended defect, here a dislocation, as usually  
27 done in space-charge models,<sup>75,77</sup> though screening effects by other vacancies are neglected in our  
28 approach (because the only charged point defects are oxygen vacancies and the electrons are delocalized  
29 through the entire model). Here, however, we are able to retain atomistic detail and drop unrealistic  
30 assumptions such as the step-wise nature of the change in vacancy formation energy<sup>77</sup>. The formation of  
31 a space-charge zone has important consequences for the electronic and ionic conductivity of this  
32 material.<sup>20,75,77,79</sup>  
33  
34

35 We now discuss our results on oxide ion diffusivity in the vicinity of a dislocation, a problem that has  
36 recently attracted much attention,<sup>5,20,22,24,71</sup> particularly in the SOFC field, where enhancing the ionic  
37 conductivity by applying elastic strain is being considered. Here we have found a different behavior  
38 depending on the vacancy concentration. For slightly reduced (or even stoichiometric) SrTiO<sub>3</sub> with an  
39 equilibrated distribution of oxygen vacancies (sample I), diffusion is confined to the vicinity of the  
40 dislocation.  
41  
42

dislocation cores because of accumulation of all vacancies to the dislocation core. The regions away from the dislocation have no oxygen vacancies, therefore the diffusion coefficient is zero (see Table 2). However, as shown above, the increased diffusion coefficient observed at the dislocation core does not imply that the dislocations are fast pipe diffusion pathways in  $\text{SrTiO}_3$ . NEB calculations show that migration barrier of oxygen vacancies at the dislocation core (up to 2 eV) is higher than that in dislocation-free bulk  $\text{SrTiO}_3$  (0.9 eV), as summarized in Table 2. Furthermore, we also find strong evidence of vacancy association, i.e. the initial and final configuration of the migration pathways do not have the same energy, the difference being up to 1.9 eV. This high association energy, which effectively increases the migration barrier, is expected to severely limit the mobility of oxygen vacancies, especially at lower temperatures.<sup>90</sup> Since pipe-diffusion is defined as a reduction in the migration energy barrier<sup>28</sup> ( $E_m$  in equation 1), *our results provide no evidence of pipe-diffusion in  $\text{SrTiO}_3$ .* The higher diffusion coefficient at the dislocation core is due solely to a higher vacancy concentration, i.e. a larger  $[V_o^*]$  and not a larger mobility,  $\exp(-E_m / k_B T)$ , in Equation 1.

The second regime studied in this paper is when the vacancy concentration is high (0.5-2.5 % range), a situation that is more relevant to SOFC applications. In this regime, vacancies are more homogeneously distributed across the material and oxide ion diffusion is observed throughout the material. The diffusion coefficients, however, do vary from one zone to the other, primarily because of the tensile and compressive uniaxial strain present in the modeled system (see Figures 1 and 8). Indeed, this can be seen in the migration energies reported in Table 4 that are lower/higher in the tensile/compressive part. The migration energy of oxide-ions in the core region is  $0.87 \pm 0.05$  eV which is analogous to that of dislocation-free bulk  $\text{SrTiO}_3$  (0.93 eV). This implies that no significant enhancement of the oxide ion diffusion coefficient is expected even at lower temperatures, i.e. *there is no evidence of pipe-diffusion* in this regime either. We note that the authors of this paper have recently studied another oxide material, doped  $\text{CeO}_2$ , which also presents an oxygen-vacancy mediated conduction mechanism, and found no evidence of pipe-diffusion along an edge dislocation.<sup>22</sup> The absence of fast diffusion along the dislocations seems therefore a common feature of these heavily reduced and/or doped oxide materials.

Finally, we would like to discuss the implications of our results for the field of fast oxide ion conductors that benefit technologies such as SOFCs, separation membranes and electrolyzers. Perovskite oxides are widely studied for these applications as materials that can serve for fast ion and electron conduction as well as for catalyzing the oxygen reduction reaction (ORR)<sup>31</sup>. Much research efforts have been dedicated to increase the ORR kinetics at lower temperatures (reduced from 800 °C to about 500 °C) to improve the performance of electrochemical devices<sup>10,91,92</sup>. To this end, Kuklja et al. showed that the ORR kinetics in

most perovskite oxides depends on the factor  $D_v \cdot [V_o^*]$ , where  $[V_o^*]$  is the oxygen vacancy concentration and  $D_v$  is the vacancy diffusion coefficient.<sup>93</sup> Our results show that dislocations significantly facilitate the creation of oxygen vacancies (i.e. they can increase  $[V_o^*]$ ) in a prototypical perovskite oxide, SrTiO<sub>3</sub>. Therefore, we suggest that a larger density of dislocations close to the material's surface might accelerate the ORR kinetics on perovskite oxides, though one would have to consider the effect of these dislocations also on surface cation composition and electronic structure.

## Conclusions

In this paper, we assessed the role of <100>{011} edge dislocations on the defect chemistry and oxide ion transport properties of SrTiO<sub>3</sub> by performing atomistic simulations. We found that in SrTiO<sub>3</sub> oxygen vacancies close to the dislocation core have lower formation energies, by as much as 2 eV. The reason for this easier reducibility lies in the strong under-coordination of the oxygen ions at the core. Ability to map out the oxygen vacancy formation energies at the atomic scale for the case of reduced dislocation cores also allowed us to visualize the formation of a space-charge zone around the dislocation and to estimate its length to be 32-40 nm, in agreement with previous experimental work.<sup>20,75</sup>

Oxide ion diffusion was studied by means of MD simulations and NEB calculations. We assessed two regimes, one with a low vacancy concentration (ppm level, relevant to resistive switching applications) and one with higher concentrations (0.5% and 2.5%, relevant to fuel cell applications). In both cases, pipe-diffusion (i.e. enhanced oxide ion mobility) is not present at the dislocation core in SrTiO<sub>3</sub>. In the low vacancy concentration regime, however, oxygen vacancy accumulation at the core gives rise to a higher diffusion coefficient, even though the migration energy barrier is higher along the dislocation core compared to that in the bulk dislocation-free SrTiO<sub>3</sub>. The extent of this vacancy accumulation, and thus the variation in total oxide ion conductivity, can be impacted kinetically by temperature and dislocation density.

The results reported here have important implications, especially in view of the technological importance of SrTiO<sub>3</sub>. As reviewed by Szot et al.<sup>2</sup>, it is true that the electrical properties of dislocations control the resistive switching behavior of SrTiO<sub>3</sub>. However, we were able to demonstrate that dislocations induce local changes of electrical properties not because of the preferably faster kinetics of oxygen migration (pipe diffusion) as previously thought<sup>2</sup>, but simply because of the structure-driven easier reducibility. This result is key for the resistive switching mechanism, and provides a quantitative and direct explanation for the electronic conductivity of dislocations in SrTiO<sub>3</sub> and related oxides studied for resistive switching. Our calculations also provided a clear atomistic picture of space charge zone around the dislocation in this

material, and the same approach can be easily used for investigating space charge effects in other materials with extended defects.

Our work has also important ramifications for other fields. The absence of pipe diffusion along dislocations in SrTiO<sub>3</sub>, an archetypical perovskite oxide, is important in quantitatively interpreting the experimental results aiming to assess the effects of strain, which sometimes include both elastic and plastic strain components, in oxide ion conductivity in oxides for energy applications. While here, and in ref.<sup>22</sup>, we demonstrated that an edge dislocation does not increase the oxide ion mobility, previous works of Kushima and Yildiz,<sup>86</sup> De Souza et al.,<sup>85</sup> Burbano et al.<sup>60</sup> and Mayeshiba and Morgan,<sup>89</sup> in related materials, have shown that *elastic* strain can increase the oxide ion mobility by reducing the migration barriers. Finally, our calculations show that a larger density of dislocations close to the material's surface might accelerate the oxygen exchange kinetics on perovskite oxides, a strategy that might be worth pursuing to further enhance the performance of these materials in fuel cells.

## 5. Acknowledgements

Authors greatly acknowledge financial support for this research from the DoE Basic Energy Sciences (DE-SC0002633). This work used the Extreme Science and Engineering Discovery Environment (XSEDE), which is supported by National Science Foundation grant number TG-DMR110004. This research used resources of the National Energy Research Scientific Computing Center, a DOE Office of Science User Facility supported by the Office of Science of the U.S. Department of Energy under Contract No. DE-AC02-05CH11231. We thank Dr. Mostafa Youssef on useful discussions related to defect chemistry and space charge in oxides and for calculating the dielectric constant of SrTiO<sub>3</sub> in this paper. We also thank Dr. Roger De Souza for clarifying some technical aspects of his previous work in modeling reduced SrTiO<sub>3</sub><sup>51</sup> and for helpful discussions on space-charge effects in this material. DM would like to thank Dr. Pierre Hirel for helpful discussions and sharing his amazing Atomsk software ([http://pierrehirel.info/codes\\_atomsk.php?lang=eng](http://pierrehirel.info/codes_atomsk.php?lang=eng)) to generate and manipulate input files. DM thanks Alex Kohlmeyer and Steve Plimpton for support with certain functions in LAMMPS.

## References

- (1) Jin, L.; Guo, X.; Jia, C. L. *Ultramicroscopy* **2013**, *134*, 77.
- (2) Szot, K.; Bihlmayer, G.; Speier, W. In *Solid State Physics*; Robert E. Camley and Robert L. Stamps, Ed.; Academic Press, 2014; Vol. Volume 65, pp 353–559.

- (3) Chen, C. H.; Kiguchi, T.; Saiki, A.; Wakiya, N.; Shinozaki, K.; Mizutani, N. *Appl. Phys. Mater. Sci. Process.* **2003**, *76*, 969.
- (4) Song, K.; Schmid, H.; Srot, V.; Gilardi, E.; Gregori, G.; Du, K.; Maier, J.; Aken, P. A. van. *APL Mater.* **2014**, *2*, 032104.
- (5) Yildiz, B. *MRS Bull.* **2014**, *39*, 147.
- (6) Chang, C.-P.; Chu, M.-W.; Jeng, H. T.; Cheng, S.-L.; Lin, J. G.; Yang, J.-R.; Chen, C. H. *Nat. Commun.* **2014**, *5*.
- (7) Wang, L.; Xu, Z.; Wang, W.; Bai, X. *J. Am. Chem. Soc.* **2014**, *136*, 6693.
- (8) Sneed, B. T.; Brodsky, C. N.; Kuo, C.-H.; Lamontagne, L. K.; Jiang, Y.; Wang, Y.; Tao, F. (Feng); Huang, W.; Tsung, C.-K. *J. Am. Chem. Soc.* **2013**, *135*, 14691.
- (9) Farmanesh, S.; Ramamoorthy, S.; Chung, J.; Asplin, J. R.; Karande, P.; Rimer, J. D. *J. Am. Chem. Soc.* **2014**, *136*, 367.
- (10) Wachsman, E.; Ishihara, T.; Kilner, J. *MRS Bull.* **2014**, *39*, 773.
- (11) Trovarelli, A.; Fornasiero, P. *Catalysis by Ceria and Related Materials*, 2nd edition edition.; Imperial College Press: London, 2013.
- (12) Waser, R.; Dittmann, R.; Staikov, G.; Szot, K. *Adv. Mater.* **2009**, *21*, 2632.
- (13) Pijolat, C.; Pupier, C.; Sauvan, M.; Tournier, G.; Lalauze, R. *Sens. Actuators B Chem.* **1999**, *59*, 195.
- (14) Manthiram, A. *J. Phys. Chem. Lett.* **2011**, *2*, 176.
- (15) Snaith, H. J. *J. Phys. Chem. Lett.* **2013**, *4*, 3623.
- (16) Riffat, S. B.; Ma, X. *Appl. Therm. Eng.* **2003**, *23*, 913.
- (17) Ramesh, R.; Spaldin, N. A. *Nat. Mater.* **2007**, *6*, 21.
- (18) Gao, P.; Britson, J.; Nelson, C. T.; Jokisaari, J. R.; Duan, C.; Trassin, M.; Baek, S.-H.; Guo, H.; Li, L.; Wang, Y.; Chu, Y.-H.; Minor, A. M.; Eom, C.-B.; Ramesh, R.; Chen, L.-Q.; Pan, X. *Nat. Commun.* **2014**, *5*.
- (19) Sillassen, M.; Eklund, P.; Pryds, N.; Johnson, E.; Helmersson, U.; Böttiger, J. *Adv. Funct. Mater.* **2010**, *20*, 2071.
- (20) Metlenko, V.; Ramadan, A.; Gunkel, F.; Du, H.; Schraknepper, H.; Hoffmann-Eifert, S.; Dittmann, R.; Waser, R.; Souza, R. D. *Nanoscale* **2014**.
- (21) McKenna, K. P. *J. Am. Chem. Soc.* **2013**, *135*, 18859.
- (22) Sun, L.; Marrocchelli, D.; Yildiz, B. *Nat. Commun.* **2015**, *6*, 6294.
- (23) Dholabhai, P. P.; Pilania, G.; Aguiar, J. A.; Misra, A.; Uberuaga, B. P. *Nat. Commun.* **2014**, *5*.
- (24) Murphy, S. T.; Jay, E. E.; Grimes, R. W. *J. Nucl. Mater.* **2014**, *447*, 143.
- (25) Curtin, W. A.; Olmsted, D. L.; Hector, L. G. *Nat. Mater.* **2006**, *5*, 875.
- (26) Legros, M.; Dehm, G.; Arzt, E.; Balk, T. J. *Science* **2008**, *319*, 1646.
- (27) Huang, J.; Meyer, M.; Pontikis, V. *Phys. Rev. Lett.* **1989**, *63*, 628.
- (28) In *Diffusion in Solids*; Springer Series in Solid-State Sciences; Springer Berlin Heidelberg, 2007; pp 583–591.
- (29) Swallow, J. G.; Woodford, W. H.; Chen, Y.; Lu, Q.; Kim, J. J.; Chen, D.; Chiang, Y.-M.; Carter, W. C.; Yildiz, B.; Tuller, H. L.; Vliet, K. J. *J. Electroceramics* **2014**, *32*, 3.
- (30) Chen, Y.; Jung, W.; Cai, Z.; Kim, J. J.; Tuller, H. L.; Yildiz, B. *Energy Environ. Sci.* **2012**, *5*, 7979.
- (31) Jung, W.; Tuller, H. L. *Adv. Energy Mater.* **2011**, *1*, 1184.
- (32) Thiel, S.; Hammerl, G.; Schmehl, A.; Schneider, C. W.; Mannhart, J. *Science* **2006**, *313*, 1942.
- (33) Mannhart, J.; Schlom, D. G. *Science* **2010**, *327*, 1607.
- (34) Muenstermann, R.; Menke, T.; Dittmann, R.; Waser, R. *Adv. Mater.* **2010**, *22*, 4819.
- (35) Jiang, W.; Kamaladasa, R. J.; Lu, Y. M.; Vicari, A.; Berechman, R.; Salvador, P. A.; Bain, J. A.; Picard, Y. N.; Skowronski, M. *J. Appl. Phys.* **2011**, *110*, 054514.
- (36) Kamaladasa, R. J.; Noman, M.; Chen, W.; Salvador, P. A.; Bain, J. A.; Skowronski, M.; Picard, Y. N. *J. Appl. Phys.* **2013**, *113*, 234510.
- (37) Messerschmitt, F.; Kubicek, M.; Schweiger, S.; Rupp, J. L. M. *Adv. Funct. Mater.* **2014**, *24*, 7448.
- (38) Ohly, C.; Hoffmann-Eifert, S.; Guo, X.; Schubert, J.; Waser, R. *J. Am. Ceram. Soc.* **2006**, *89*, 2845.
- (39) Moos, R.; Meneskou, W.; Härdtl, K. H. *Appl. Phys. A* **1995**, *61*, 389.
- (40) Balachandran, U.; Eror, N. G. *J. Solid State Chem.* **1981**, *39*, 351.
- (41) Lin, C.; Demkov, A. A. *Phys. Rev. Lett.* **2013**, *111*.
- (42) Tanaka, T.; Matsunaga, K.; Ikuhara, Y.; Yamamoto, T. *Phys. Rev. B* **2003**, *68*.
- (43) Cuong, D.; Lee, B.; Choi, K.; Ahn, H.-S.; Han, S.; Lee, J. *Phys. Rev. Lett.* **2007**, *98*.
- (44) Szot, K.; Speier, W.; Bihlmayer, G.; Waser, R. *Nat. Mater.* **2006**, *5*, 312.
- (45) Szot, K.; Dittmann, R.; Speier, W.; Waser, R. *Phys. Status Solidi RRL – Rapid Res. Lett.* **2007**, *1*, R86.
- (46) Wachsman, E. D.; Lee, K. T. *Science* **2011**, *334*, 935.

- (47) Szot, K.; Speier, W.; Carius, R.; Zastrow, U.; Beyer, W. *Phys. Rev. Lett.* **2002**, 88.
- (48) Kilner, J. A.; Burriel, M. *Annu. Rev. Mater. Res.* **2014**, 44, 365.
- (49) Thomas, B. S.; Marks, N. A.; Begg, B. D. *Nucl. Instrum. Methods Phys. Res. Sect. B Beam Interact. Mater. At.* **2005**, 228, 288.
- (50) Thomas, B.; Marks, N.; Harrowell, P. *Phys. Rev. B* **2006**, 74.
- (51) Schie, M.; Marchewka, A.; Müller, T.; De Souza, R. A.; Waser, R. *J. Phys. Condens. Matter* **2012**, 24, 485002.
- (52) Hirel, P.; Marton, P.; Mrovec, M.; Elsässer, C. *Acta Mater.* **2010**, 58, 6072.
- (53) Hirel, P.; Mrovec, M.; Elsässer, C. *Acta Mater.* **2012**, 60, 329.
- (54) Uberuaga, B. P.; Choudhury, S.; Bai, X.-M.; Benedek, N. A. *Scr. Mater.* **2012**, 66, 105.
- (55) Benedek, N. A.; Chua, A. L.-S.; Elsässer, C.; Sutton, A. P.; Finnis, M. W. *Phys. Rev. B* **2008**, 78, 064110.
- (56) Chua, A. L.-S.; Benedek, N. A.; Chen, L.; Finnis, M. W.; Sutton, A. P. *Nat. Mater.* **2010**, 9, 418.
- (57) Bishop, S. R.; Marrocchelli, D.; Chatzichristodoulou, C.; Perry, N. H.; Mogensen, M. B.; Tuller, H. L.; Wachsman, E. D. *Annu. Rev. Mater. Res.* **2013**, 44, 140228162707002.
- (58) Plimpton, S. *J. Comput. Phys.* **1995**, 117, 1.
- (59) Hockney, R. W.; Eastwood, J. W. *Computer Simulation Using Particles*; CRC Press: Bristol England ; Philadelphia, 1989.
- (60) Burbano, M.; Marrocchelli, D.; Watson, G. W. *J. Electroceramics* **2014**, 32, 28.
- (61) Burbano, M.; Nadin, S.; Marrocchelli, D.; Salanne, M.; Watson, G. W. *Phys. Chem. Chem. Phys.* **2014**, 16, 8320.
- (62) Marrocchelli, D.; Madden, P. A.; Norberg, S. T.; Hull, S. *Chem. Mater.* **2011**, 23, 1365.
- (63) Norberg, S. T.; Hull, S.; Ahmed, I.; Eriksson, S. G.; Marrocchelli, D.; Madden, P. A.; Li, P.; Irvine, J. T. S. *Chem. Mater.* **2011**, 23, 1356.
- (64) Burbano, M.; Norberg, S. T.; Hull, S.; Eriksson, S. G.; Marrocchelli, D.; Madden, P. A.; Watson, G. W. *Chem. Mater.* **2012**, 24, 222.
- (65) Jia, C.; Thust, A.; Urban, K. *Phys. Rev. Lett.* **2005**, 95.
- (66) Jia, C. L.; Houben, L.; Urban, K. *Philos. Mag. Lett.* **2006**, 86, 683.
- (67) Enterkin, J. A.; Subramanian, A. K.; Russell, B. C.; Castell, M. R.; Poeppelmeier, K. R.; Marks, L. D. *Nat. Mater.* **2010**.
- (68) Ertekin, E.; Srinivasan, V.; Ravichandran, J.; Rossen, P. B.; Siemons, W.; Majumdar, A.; Ramesh, R.; Grossman, J. C. *Phys. Rev. B* **2012**, 85.
- (69) Ahn, K.; Chung, Y.-C.; Yoon, K. J.; Son, J.-W.; Kim, B.-K.; Lee, H.-W.; Lee, J.-H. *J. Electroceramics* **2014**, 32, 72.
- (70) Rupp, J. L. M.; Fabbri, E.; Marrocchelli, D.; Han, J.-W.; Chen, D.; Traversa, E.; Tuller, H. L.; Yildiz, B. *Adv. Funct. Mater.* **2014**, 24, 1562.
- (71) Zhang, F.; Walker, A. M.; Wright, K.; Gale, J. D. *J. Mater. Chem.* **2010**, 20, 10445.
- (72) Kuru, Y.; Marrocchelli, D.; Bishop, S. R.; Chen, D.; Yildiz, B.; Tuller, H. L. *J. Electrochem. Soc.* **2012**, 159, F799.
- (73) Chueh, W. C.; McDaniel, A. H.; Grass, M. E.; Hao, Y.; Jabeen, N.; Liu, Z.; Haile, S. M.; McCarty, K. F.; Bluhm, H.; El Gabaly, F. *Chem. Mater.* **2012**, 24, 1876.
- (74) Feng, Z. A.; El Gabaly, F.; Ye, X.; Shen, Z.-X.; Chueh, W. C. *Nat. Commun.* **2014**, 5.
- (75) De Souza, R. A.; Metlenko, V.; Park, D.; Weirich, T. E. *Phys. Rev. B* **2012**, 85.
- (76) Lee, H.-S.; Mizoguchi, T.; Mistui, J.; Yamamoto, T.; Kang, S.-J. L.; Ikuhara, Y. *Phys. Rev. B* **2011**, 83.
- (77) Souza, R. A. D. *Phys. Chem. Chem. Phys.* **2009**, 11, 9939.
- (78) De Souza, R. A.; Fleig, J.; Maier, J.; Zhang, Z.; Sigle, W.; Rühle, M. *J. Appl. Phys.* **2005**, 97, 053502.
- (79) Göbel, M. C.; Gregori, G.; Maier, J. *Phys. Chem. Chem. Phys.* **2014**, 16, 10214.
- (80) Denk, I.; Münch, W.; Maier, J. *J. Am. Ceram. Soc.* **1995**, 78, 3265.
- (81) Islam, M. S. *Solid State Ion.* **2002**, 154, 75.
- (82) Islam, M. S.; Davies, R. A. *J. Mater. Chem.* **2004**, 14, 86.
- (83) Huang, K.; Tichy, R. S.; Goodenough, J. B. *J. Am. Ceram. Soc.* **1998**, 81, 2565.
- (84) Stäuble-Pümpin, B.; Ilge, B.; Matijasevic, V. C.; Scholte, P. M. L. O.; Steinfort, A. J.; Tuinstra, F. *Surf. Sci.* **1996**, 369, 313.
- (85) De Souza, R. A.; Ramadan, A.; Hörner, S. *Energy Environ. Sci.* **2012**, 5, 5445.
- (86) Kushima, A.; Yildiz, B. *J. Mater. Chem.* **2010**, 20, 4809.
- (87) Hinterberg, J.; Zacherle, T.; De Souza, R. A. *Phys. Rev. Lett.* **2013**, 110.
- (88) Rushton, M. J. D.; Chroneos, A. *Sci. Rep.* **2014**, 4.

- 1  
2  
3 (89) Mayeshiba, T.; Morgan, D. *Phys. Chem. Chem. Phys.* **2014**,  
4 (90) Kilner, J. A. *Solid State Ion.* **2000**, *129*, 13.  
5 (91) Chen, Y.; Cai, Z.; Kuru, Y.; Ma, W.; Tuller, H. L.; Yildiz, B. *Adv. Energy Mater.* **2013**, *3*, 1221.  
6 (92) An, J.; Shim, J. H.; Kim, Y.-B.; Park, J. S.; Lee, W.; Gür, T. M.; Prinz, F. B. *MRS Bull.* **2014**, *39*, 798.  
7 (93) Kuklja, M. M.; Kotomin, E. A.; Merkle, R.; Mastrikov, Y. A.; Maier, J. *Phys. Chem. Chem. Phys.* **2013**, *15*,  
8 5443.  
9  
10  
11  
12  
13  
14  
15  
16  
17  
18  
19  
20  
21  
22  
23  
24  
25  
26  
27  
28  
29  
30  
31  
32  
33  
34  
35  
36  
37  
38  
39  
40  
41  
42  
43  
44  
45  
46  
47  
48  
49  
50  
51  
52  
53  
54  
55  
56  
57  
58  
59  
60